

NuSTAR as an Axion Helioscope

J. Ruz^{1,2*}, E. Todarello^{3,4*}, J. K. Vogel^{1,2*}, M. Giannotti^{1,11†},
B. Grefenstette⁵, H. S. Hudson^{6†}, I. G. Hannah⁶, I. G. Irastorza¹,
C. S. Kim⁷, T. O’Shea¹, M. Regis^{3,4}, D. M. Smith^{8†}, M. Taoso⁴,
J. Trujillo Bueno^{9,10}

¹Centro de Astropartículas y Física de Altas Energías, University of Zaragoza, Zaragoza, 50009, Aragón, Spain.

²Physics and Life Science Directorate, Lawrence Livermore National Laboratory, Livermore, 94550, CA, United States of America.

³Dipartimento di Fisica, University of Torino, I-10125, Torino, Italy.

⁴Istituto Nazionale di Fisica Nucleare, Sezione di Torino, I-10125, Torino, Italy.

⁵California Institute of Technology, Space Radiation Lab, Pasadena, 91125, CA, United States of America.

⁶School of Physics and Astronomy, , University of Glasgow, Glasgow, G12 8QQ, Scotland, United Kingdom.

⁷Department of Physics, University of California Santa Barbara, Santa Barbara, 93106, CA, United States of America.

⁸Physics Department and Santa Cruz Institute for Particle Physics, University of California Santa Cruz, Santa Cruz, 95064, CA, United States of America.

⁹Instituto de Astrofísica de Canarias, 38205, La Laguna, Tenerife, Spain.

¹⁰Consejo Superior de Investigaciones Científicas, Spain.

¹¹Department of Chemistry and Physics, Barry University, Miami Shores, 33161, FL, United States of America.

*Corresponding author(s). E-mail(s): Jaime.Ruz@cern.ch;
elisamaria.todarello@unito.it; Julia.Vogel@cern.ch;

Contributing authors: mgiannotti@unizar.es; bwgref@srl.caltech.edu;
hugh.hudson@glasgow.ac.uk; Iain.Hannah@glasgow.ac.uk;
irastorz@unizar.es; crystalkim@ucsb.edu; tgerard@unizar.es;
marco.regis@unito.it; dsmith8@ucsc.edu; taoso@to.infn.it; jtb@iac.es;

†These authors contributed equally to this work.

Abstract

The nature of dark matter in the Universe is still an open question in astrophysics and cosmology. Axions and axion-like particles (ALPs) offer a compelling solution, and traditionally ground-based experiments have eagerly, but to date unsuccessfully, searched for these hypothetical low-mass particles that are expected to be produced in large quantities in the strong electromagnetic fields in the interior of stars. This work offers a fresh look at axions and ALPs by leveraging their conversion into X-rays in the magnetic field of the Sun’s atmosphere rather than a laboratory magnetic field. Unique data acquired with the Nuclear Spectroscopic Telescope Array (NuSTAR) during the solar minimum in 2020 allows us to set stringent limits on the coupling of axions to photons using state-of-the-art magnetic field models of the solar atmosphere. We report pioneering limits on the axion-photon coupling strength of $6.9 \times 10^{-12} \text{ GeV}^{-1}$ at 95% confidence level for axion masses $m_a \lesssim 2 \times 10^{-7} \text{ eV}$, surpassing current ground-based searches and further probing unexplored regions of the axion-photon coupling parameter space up to axion masses of $m_a \lesssim 5 \times 10^{-4} \text{ eV}$.

Keywords: axions, ALPs, NuSTAR, axion helioscope, dark matter

Introduction

While the Standard Model (SM) of particle physics has successfully explained multiple observed phenomena and predicted experimental outcomes concerning fundamental particles and their relation to three of the four fundamental forces, it still falls short of explaining the strong charge-parity (CP) problem in quantum chromodynamics (QCD) and the nature of dark matter, amongst other problems. Interestingly, both of these questions can be addressed by a common solution, proposed over 45 years ago by R. Peccei and H. Quinn [1], which results in the existence of a low-mass, pseudo-scalar boson, the QCD axion [2–7]. Furthermore, axion-like particles (ALPs), or non-QCD axions, are invoked in various beyond-the-standard model scenarios, theoretically well-motivated at the low energy frontier of particle physics. ALPs are light pseudo-scalar particles that mix with photons similarly to axions but do not exhibit the axion-typical relation between mass m_a and the Peccei-Quinn scale $f_a \propto 1/m_a$. While ALPs might not solve the strong CP problem, they could compose all or part of the dark matter. We will use the term “axion” to refer collectively to both QCD axions and ALPs.

Numerous searches, both in the laboratory and in the sky, have been designed to look for these particles [8–10]. Experiments mostly rely on the axion coupling to photons [11], described by the effective Lagrangian term $\mathcal{L} \propto g_{a\gamma} a \mathbf{E} \cdot \mathbf{B}$, where a is the axion field, \mathbf{E} and \mathbf{B} denote the electric and magnetic fields, respectively, and $g_{a\gamma}$ is the strength of the axion-photon coupling. Such an interaction leads to the Primakoff effect —the conversion of photons into axions (and vice versa) in the presence of an electromagnetic field. Due to its vicinity, the Sun can be a bright source of axions. Relativistic axions can be produced in the solar core by Primakoff conversion of thermal X-ray photons on nuclear and electron electric fields. These axions are then converted back into photons in the magnetic field of the Sun’s atmosphere [12]. This process

leads to an axion-generated X-ray flux with distinctive spectral and spatial properties that can be exploited to distinguish it from well-known solar X-ray emission processes and instrumental background in X-ray telescopes.

Solar X-ray observations have improved steadily in resolution and sensitivity, making it possible to search for signatures from axions of solar origin. First attempts at using satellite missions as axion searches were made with the *Yohkoh*/SXT instrument [13], which operated between 1991 and 2001. Carlson & Tseng [12] used some of these data to derive first estimates on upper limits for the axion-photon coupling. More recent solar observatories, such as RHESSI [14, 15] and *Hinode*/XRT [16], were used with similar approaches. However, due to the high background rates and optimization of these instruments for bright solar X-rays, dedicated solar missions are not very suitable for weak-signal dark matter searches. NASA’s Nuclear Spectroscopic Telescope Array (NuSTAR) [17] is the first highly sensitive X-ray astronomy instrument designed to observe faint astrophysical sources while also being capable of monitoring the Sun during periods of low solar activity. With its large effective area and low background, NuSTAR achieves more sensitive limits than other observatories, as detailed in the following Sections.

Using NuSTAR solar observations, we conduct a search for axion-induced X-ray emission (see Fig. 1). We observe no evidence of an axion signal above background and therefore set upper limits on the axion-photon coupling strength, significantly improving existing bounds from laboratory searches [20–29] and matching the sensitivity of current astrophysical bounds [30–48].

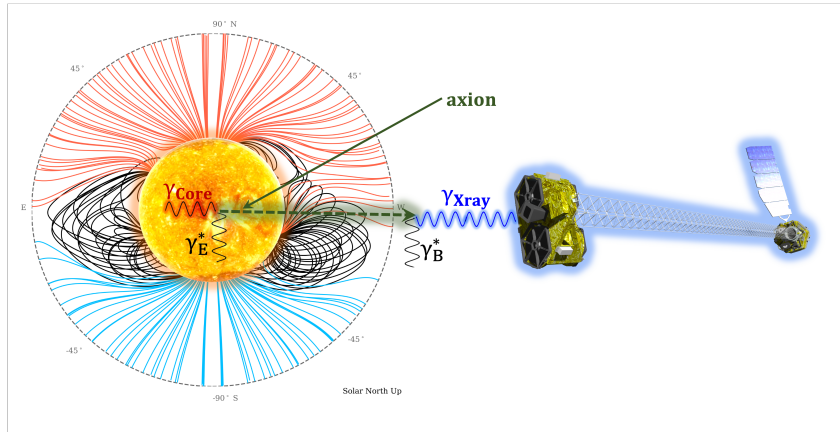


Fig. 1: NuSTAR spacecraft [18] (right) searching for X-ray photons (blue line) from axion-to-photon conversion in the solar atmosphere (left). Axions (green dashed line) are created in the hot plasma of the solar core via the Primakoff effect due to the presence of electric fields (γ_E^*) and get back-converted into X-ray photons by means of the inverse-Primakoff effect in the presence of the magnetic fields (γ_B^*) in the solar atmosphere [19].

Modeling of the Axion Flux and Solar Atmosphere

Black-body photons in the solar core are converted into axions due to the electric fields of the charged particles in the hot plasma $\gamma + (e^-, Ze) \rightarrow a + (e^-, Ze)$ [11]. The current understanding of stellar nucleosynthesis [49] provides an explanation for the energy source of the stars—the core is the only location of the Sun that produces an appreciable amount of heat via fusion reactions, e.g., the proton-proton chain. Its temperature is $T_c \sim 1.3$ keV and its dimension is about 20% of the solar radius, with an estimated density of $\rho_c \sim 1.5 \times 10^5$ kg/m³. The axion emission from the Sun's core is directly related to the temperature of its plasma, $E_a \sim 2.7 \times T_c$, due to the strong temperature dependence of the number of thermal X-rays produced. Given the temperature gradient within the Sun's interior, the axion spectrum varies with radius (see Fig. 2). The total differential axion flux from the solar core can be calculated by taking into account the standard model of the Sun and its luminosity $L_\odot = 3.85 \times 10^{33}$ erg s⁻¹ [23, 50].

The differential solar X-ray flux arising from axion-photon conversion in the Sun's atmosphere (left side of Eq. (1)) is determined by the axion flux produced in the solar interior (first term on the right-hand side of Eq. (1)), and the probability that axions convert into photons as they exit the solar atmosphere ($P_{a \rightarrow \gamma}$)

$$\frac{dN_\gamma}{dE dA dt d\Omega} = \frac{dN_a}{dE dA dt d\Omega} P_{a \rightarrow \gamma} , \quad (1)$$

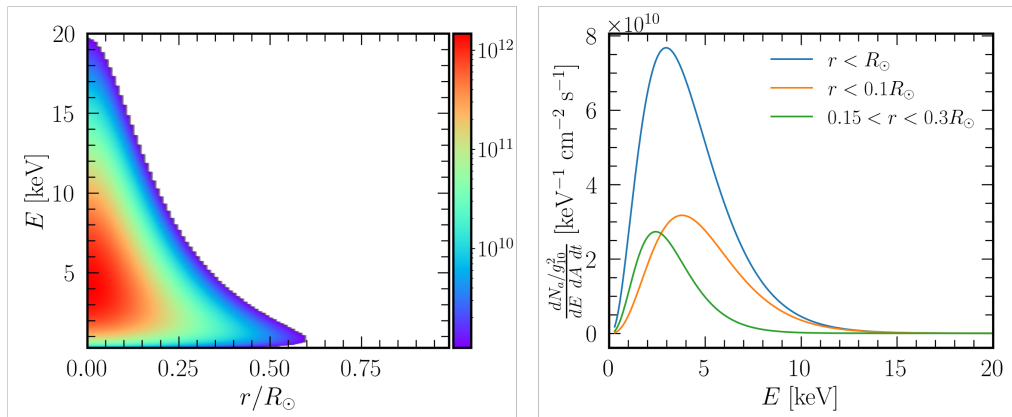


Fig. 2: Left: Solar axion surface luminosity depending on energy and the radius r/R_\odot on the solar disk. The flux ($\frac{dN_a/g_{10}^2}{dE dA dt dA_\odot}$) is given in units of axions keV⁻¹cm⁻²s⁻¹ per unit surface area on the solar disk. **Right:** Differential solar axion spectrum, derived by integrating the model shown on the left up to different values of r/R_\odot in units of the solar radius R_\odot . The total axion flux is shown in blue, while the expected axion flux from 10% of the solar radius is shown in orange. The axion signal expected in a concentric annulus comprising the 15-to-30% radius of the Sun is shown in green [23].

with dE , dA , dt , and $d\Omega$ being the elements of energy, area, time, and solid angle, respectively. As shown in Fig. 2, the resulting axion flux peaks at energies ~ 4 keV in the solar core. These features are imprinted on the spectral and morphological properties of the resulting X-ray emission in Eq. (1). Accurate theoretical calculations of the axion flux are available in the literature, and we based our analysis on the results of [50]. Since both the creation of axions from solar-core X-rays and their conversion in the magnetic field of the solar atmosphere are due to the Primakoff process, the total X-ray signal at Earth scales as $g_{a\gamma}^4$. The highly relativistic axions produced in the core emerge at the Sun's surface along approximately radial trajectories. The probability of conversion into photons is then given by¹

$$P_{a\rightarrow\gamma}(h) = \frac{1}{4} g_{a\gamma}^2 \left| \int_0^h dh' B_{\perp}(h') e^{i \int_0^{h'} dh'' q(h'')} e^{-\frac{1}{2} \int_{h'}^h dh'' \Gamma(h'')} \right|^2, \quad (2)$$

where h is the altitude from the visible surface of the Sun, B_{\perp} is the component of the magnetic field perpendicular to the direction of propagation of the photon, and $q(h) = (\omega_p^2(h) - m_a^2)/2E$ is the momentum exchanged between the photon in the medium and the axion, both carrying energy E . The plasma frequency of the medium is $\omega_p = \sqrt{e^2 n_e / m_e}$, where e and m_e are the electric charge and the mass of the electron, respectively, while n_e is the height-dependent number density of free electrons plus that of bound electrons with ionization energy much smaller than the X-ray energy. In natural units, the plasma frequency is equivalent to an effective mass of the photon.

The behavior of the probability function Eq. (2) is controlled by the functions Γ and q . The phase $\int_0^h dh' q(h')$ governs the axion-to-photon conversion. The presence of this factor may suppress the conversion probability, though there are circumstances in which this is not the case. For instance, when the phase term is constant, and thus it disappears upon squaring in Eq. (2). Further details are given in Appendix A. The term containing Γ in Eq. (2) represents the absorption between altitudes h' and h of the arising X-rays in the solar atmosphere [52, 53].

The properties of the conversion depend sensitively upon the Sun's atmospheric structure —specifically on its magnetic field and plasma density. Previous works have made use of different approximations for the model of the solar magnetic field and plasma density. For example, [12] used a global dipole model of the solar field, while [15] and [16] used the 1D semi-empirical model VAL-C [54] in combination with plausible *ad hoc* assumptions about the magnetic field. Here, we extract our magnetic field model from realistic state-of-the-art MHD simulations, representative of the quiet Sun atmosphere, which is the appropriate condition for the solar NuSTAR observations. The magnetic field model used in this work is shown on the top panel of Fig. 3 as a function of the height above the Sun's visible surface.

At low altitudes, below 400 km, we used the model from [55], obtained with the MURaM radiative MHD code [57, 58], which resulted from a magneto-convection simulation with small-scale dynamo action. This three-dimensional (3D) model has periodic boundary conditions in the horizontal plane perpendicular to the solar radius

¹We use natural ($c = \hbar = 1$) and Heaviside-Lorentz ($\epsilon_0 = \mu_0 = 1$) units. Magnetic fields are converted to these units as $1 \text{ Gauss} = 1.953 \times 10^{-2} \text{ eV}^2$ [51].

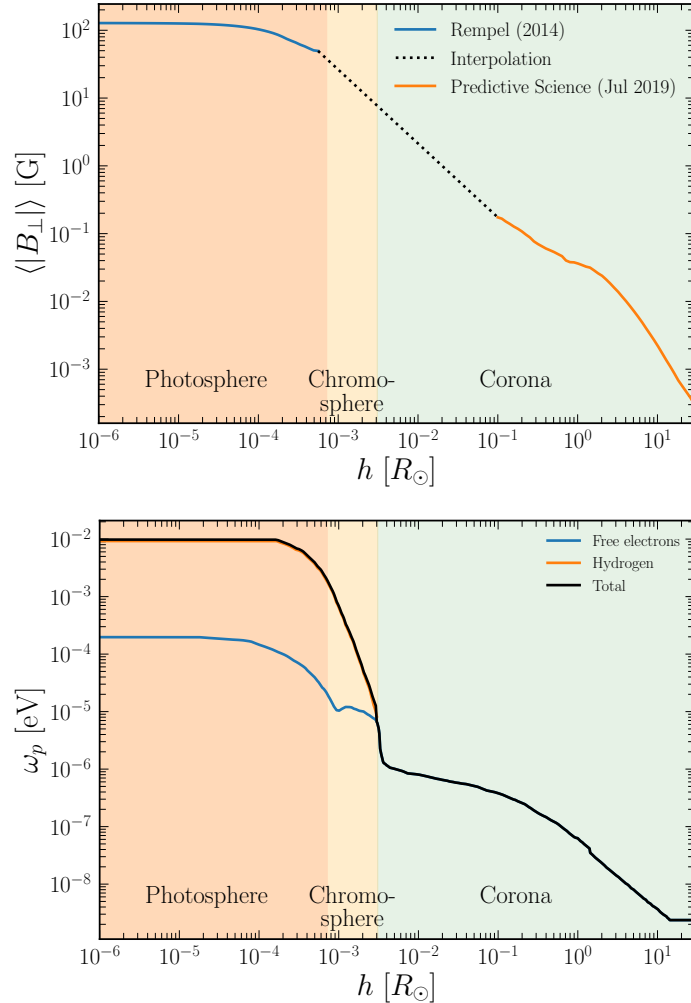


Fig. 3: Top: Modeling of the transverse component of the solar atmospheric magnetic field: Rempel [55] (blue line), Predictive science [56] (orange line), and power-law interpolation between both models (dashed black line). **Bottom:** Contributions to axion plasma frequency from free electrons (blue line), hydrogen (orange line), and total added contribution (black line). **In both view-graphs:** shaded regions for the photosphere (orange), chromosphere (yellow), and corona (green).

vector through the observed point on the solar disk. This model of the solar photosphere is representative of the “quiet” inter-network regions of the solar visible surface, which occupy most of the solar disk at any given time during the solar activity cycle. The magnetic field of this 3D model is rather tangled at scales below the spatial resolution of today’s solar telescopes and has a mean field strength of 170 Gauss at the model’s visible surface. It produces a depolarization of the linear polarization signals

in photospheric spectral lines that agrees with observations [59, 60]. The blue curve on the top panel of Fig. 3 shows the variation with height of $\langle |B_{\perp}| \rangle$, calculated at each height in the model by spatially averaging the $|B_{\perp}|$ values of all points in the horizontal plane perpendicular to the solar radius vector.

For the coronal magnetic field, we use the publicly available model from the Predictive Science Inc. (PSI) MHD simulation relative to the July 2nd, 2019 solar eclipse [56], when the Sun was in a quiet phase, as it was during our observation (see Appendix C.1 for more details). The PSI simulation provides a three-dimensional model of the coronal magnetic field up to an altitude $h = 29R_{\odot}$. To extract $\langle |B_{\perp}| \rangle$, we determine from the 3D model the component of the magnetic field perpendicular to the line of sight from Earth pointing towards the center of the Sun, averaged over a perpendicular disk of radius $0.1R_{\odot}$, corresponding to our signal region. We repeat this procedure 120 times, successively rotating the model by an azimuthal angle of 3° . Finally, for each h , we take the median of the 120 possible values of $\langle |B_{\perp}| \rangle$ to obtain the result shown by the orange line on the top panel of Fig. 3.

The Predictive Science simulation does not have the resolution to determine the behavior of the magnetic field below $h \sim 0.1R_{\odot}$, while the model from [55] is reliable for $h < 400$ km. There is no firm knowledge of the magnetic field between these two regions. Therefore, we choose a simple power law interpolation, indicated in the top part of Fig. 3 by a dotted line. The resulting perpendicular magnetic field strength is about 1.4 G at an altitude of 10,000 km. The magnetic field in this region is most relevant to the conversion probability for ALP masses $\gtrsim 10^{-4}$ eV.

For the free electron and hydrogen density, we use the model from [61], also representative of the quiet Sun. This model is, in turn, based on model VAL-C of the chromosphere from [54] and the coronal model by [62]. Our approach describes only the quiet Sun and ignores the additional coronal density associated with the streamer belt. In addition to free electrons and hydrogen, we consider the contribution to the plasma density from helium (He). We assume that its density profile follows the one of hydrogen (H) and take a relative abundance $n_{\text{H}}/n_{\text{He}} = 0.06$ [63–65]. We do not include the contribution of heavier elements to the plasma frequency since it is negligible given their low abundances. In the chromosphere, the ionization fraction is small, and the plasma frequency results from the density of electrons bound to atoms, mainly hydrogen, as shown on the bottom panel of Fig. 3. In the corona, the temperature is of order 10^6 K, implying that hydrogen and helium are fully ionized. Due to their higher mass, the contribution from nuclei to the plasma frequency is suppressed compared to that of free electrons.

The absorption coefficient is given by the sum over i of $\Gamma_i = n_i \sigma_i$, where n_i is the number density of species i and σ_i is the total photon cross-section on species i . To compute Γ , we consider all elements up to an atomic number $Z = 30$. The element abundances are taken from the CHIANTI database [66, 67]. In particular, we use the Schmelz extended model of coronal abundances, derived from [63–65]. For each element, we take the total photon cross-section from the XCOM database by NIST [68]. The processes involved in the X-ray attenuation are coherent (Rayleigh) and incoherent (Compton) scattering, as well as photoelectric absorption.

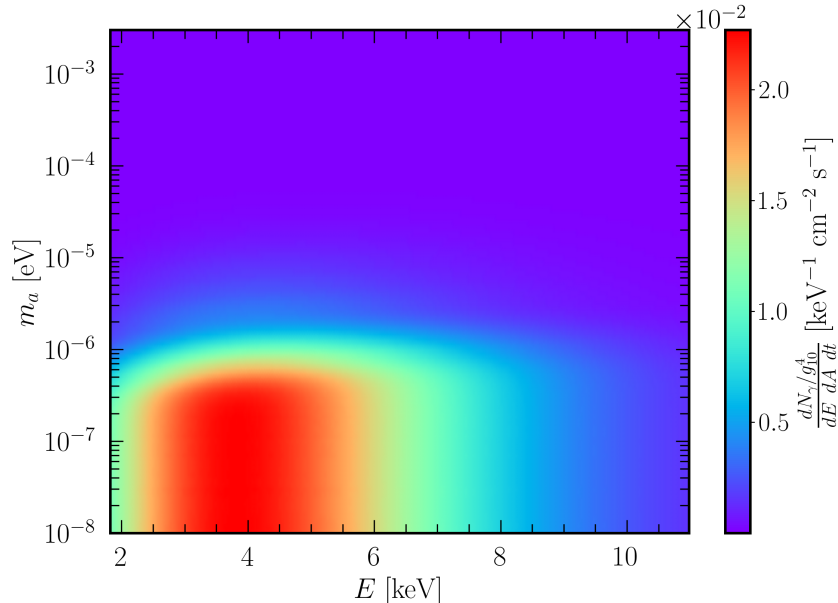


Fig. 4: Number of photons due to axion conversion per unit energy, area and time, for an axion-to-photon coupling $g_{10} = 1$, where $g_{10} = g_{a\gamma}/(10^{-10} \text{ GeV}^{-1})$.

In Eq. (2), the integration starts from $h = 0$ and extends up to an altitude $h = 29R_{\odot}$, which is where our models stop and which is well above the height at which $P_{a\gamma}$ saturates. Fig. 4 shows the expected signal as a function of the axion mass and of the X-ray energy. This is obtained by integrating Eq. (1) over the signal region discussed in the next Section. We can see that, as expected, the signal peaks at around 4 keV. As discussed in detail in Appendix A, the conversion probability grows as the plasma density drops until the resonance condition is met at the location where $m_a = \omega_p$. At altitudes sufficiently larger than the resonance location, $P_{a\gamma}$ does not grow anymore but rather oscillates about a constant value. For masses smaller than 10^{-6} eV, the resonance condition $m_a = \omega_p$ is achieved well inside the corona in regions where the magnetic field is quickly dropping or at altitudes beyond those covered by our model. This implies that the presence of a resonance has a mild impact on $P_{a\gamma}$. For higher masses, the resonance condition is met at lower and lower altitudes, stopping the growth of $P_{a\gamma}$ earlier. This explains the drop in the photon counts for $m_a \gtrsim 10^{-6}$ eV seen in Figure 4.

NuSTAR observations

Data for our solar observations were acquired using the Nuclear Spectroscopic Telescope Array (NuSTAR), a NASA small-explorer (SMEX) mission [17]. NuSTAR uses two grazing-incidence telescope modules focusing X-rays in the range of 3 – 79 keV onto two focal plane detectors, which are pixelated cadmium zinc telluride (CdZnTe)

sensors. Thanks to the mirror coatings and the detector configuration, NuSTAR is the first focusing X-ray telescope for hard X-rays in space, superior to other astrophysical X-ray telescopes at high energies. The ability to point at the Sun makes this mission a unique instrument among focusing X-ray telescopes, and since September 2014, a little over two years after launch, NuSTAR’s annual observing program has included pointings to the Sun for the study of active regions, X-ray bright points, and flares [69].

On 21 February 2020, NuSTAR was pointed to the solar disk center for 23,307 seconds of live exposure for the joint purposes of conducting a solar axion search, and the study of X-ray bright points on the solar photosphere [70]. The timing coincided with the minimum of the 11-year cycle of solar activity, which benefited both projects by eliminating interference from bright solar active regions or solar flares in or out of the $12' \times 12'$ field of view. To look for the predicted axion spectrum, the counts in the pixels within 0.1 solar radii ($1.6'$) of the disk center were accumulated, while an annulus from 0.15 to 0.30 solar radii was used to accumulate a background spectrum. Below 3 keV, the background is dominated by emission from the solar atmosphere and X-ray bright points [70], but above 4.5 keV it is dominated by “stray light” – cosmic photons that have not interacted in the optics – and detector-intrinsic radioactivity, and is fairly uniform on the detector plane in the 4–15 keV energy range. Figure 5 (left panel) shows the total counts in the signal region as a function of energy (red dots), along with the background (cyan line) derived from the outer annular region, re-scaled by the respective areas of the regions, smoothed with a running polynomial fit, and adjusted slightly for the known gradient of cosmic background X-rays across the detector chips (see Appendix B). The right panel shows the subtracted spectrum (grey dots) and expected axion flux for the obtained 95% confidence level (C.L.) limit (grey line).

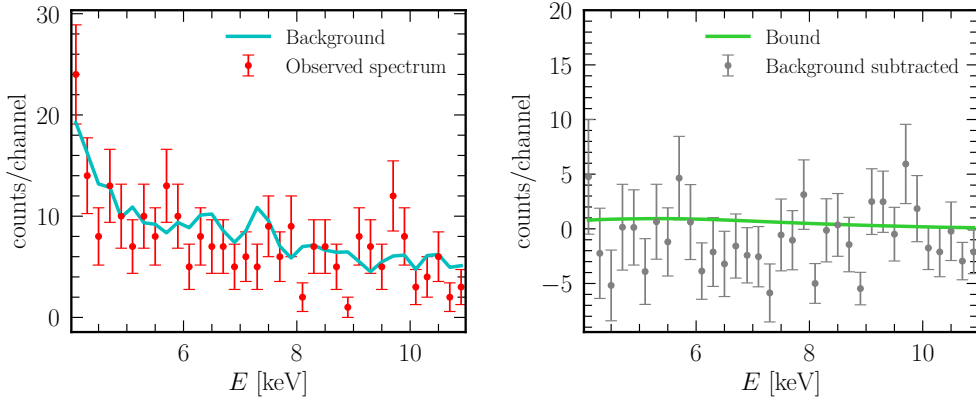


Fig. 5: **Left:** NuSTAR observed spectrum in the signal region (red) in comparison with the area-scaled background spectrum (cyan). Data have been rebinned from raw 0.04 keV bins to 0.2 keV bins for display purposes. **Right:** Background-subtracted spectrum (grey dots) and spectral shape of the axion component folded through the instrument response. The spectrum from axion conversion with $g_{a\gamma}$ set to the 95% upper limit (green line) is shown for an axion mass of $m_a = 10^{-7}$ eV.

of $g_{a\gamma}$ (green line). For clarity, we have opted to plot the obtained background spectra without its statistical uncertainty. This decision is based upon the fact that the overall statistical error of the background is about a factor two smaller than the statistical uncertainty associated with the observed spectrum in the signal region. In fact, an important feature of our data treatment is that the detector background is measured over an area 5.3 times larger than the signal region. The use of these data to estimate and subtract the true experimental background (grey dots of right panel in Fig. 5) is the most sensitive step in the NuSTAR analysis.

Details on the data processing and preparation for the NuSTAR solar data (Observation IDs 80512218001, 8051222X001 with $X = 0, 1 - 6, 8$) can be found in Appendix B. The processing of the data is based on the standard NuSTAR Data Analysis Software (NuSTARDAS) version 2.0.0 with calibration database (CALDB) version 20209012 and has been expanded to account for the special case of solar observations. The same Appendix furthermore discusses details of the background selection and scaling.

Data Analysis

The expected number of photons from axion conversion in a given NuSTAR energy bin i coming from the region j is

$$N_{\gamma}^{ax,j}(E_i) = A_{\text{eff}}^j(E_i) \Delta t \int_{E_i - \Delta E/2}^{E_i + \Delta E/2} dE \epsilon_{\text{NS}}(E) \frac{dN_a^j}{dA dt dE}(E) P_{a \rightarrow \gamma}(E) , \quad (3)$$

where A_{eff}^j is the telescope effective area [71], $\Delta t = 23,307$ s is the duration of the observation (live time), ΔE is the width in energy of each bin (40 eV), and ϵ_{NS} is the NuSTAR energy response function described in [72]. The label $j = s, b$ indicates signal ($r < 0.1R_{\odot}$) or background ($0.15R_{\odot} < r < 0.3R_{\odot}$) regions.

The axion flux from Primakoff conversion in the Sun's core [23] is shown on the left panel of Fig. 2. A_{\odot} represents the transverse area of the solar disk, expressed in units of R_{\odot}^2 . The right panel of Fig. 2 shows the total axion flux and the axion flux arising from our signal and background regions.

The total number of X-ray photons expected in the signal region is

$$N_{\gamma}^s = N_{\gamma}^{ax,s} + N_{\gamma}^{B,s} , \quad (4)$$

where $N_{\gamma}^{B,s}$ refers to the background X-ray emission in the signal region, i.e., radiation produced by processes other than the axion conversion. To determine $N_{\gamma}^{B,s}$, we use photon counts in the background region as follows.

We assume that the number of background X-ray photons per unit area is constant across the Sun's disk. Then, we can write

$$N_{\gamma}^{B,s} = N_{\gamma}^{B,b} \frac{A_{\odot}^s}{A_{\odot}^b} = (N_{\gamma}^b - N_{\gamma}^{ax,b}) \frac{A_{\odot}^s}{A_{\odot}^b} , \quad (5)$$

where N_γ^b is the number of detected photons in the background region, while A_\odot^s and A_\odot^b are the transverse areas of the signal and background regions, respectively. Therefore, the total number of X-ray photons expected in the signal region and in an energy bin i can be rearranged as

$$\lambda_i \equiv N_\gamma^s = b_i + g_{10}^4 \nu_i , \quad (6)$$

with signal

$$\nu_i \equiv N_\gamma^{ax,s}(E_i) - N_\gamma^{ax,b}(E_i) \frac{A_\odot^s}{A_\odot^b} , \quad (7)$$

and background

$$b_i \equiv N_\gamma^b \frac{A_\odot^s}{A_\odot^b} . \quad (8)$$

In Eq. (6), $g_{10} \equiv g_{a\gamma}/10^{-10} \text{ GeV}^{-1}$. We assume independent Poisson statistics in each energy bin and compute the likelihood as

$$\mathcal{L} \propto \prod_i \frac{e^{-\lambda_i} \lambda_i^{n_i}}{n_i!} , \quad (9)$$

where n_i is the number of photons detected in the i -bin. To extract our limit, we consider the energy range from 4 to 11 keV and apply the prior $\Theta(g_{10}^4)$, where Θ is the Heaviside step function. We integrate the Bayesian posterior probability density function (PDF) from zero to the point where it encompasses 95% of the total PDF area.

The overall systematic error on the limit presented is discussed in the Supplemental Material (see Appendix C.2). We take into consideration not only the model uncertainties of the solar atmosphere magnetic field, our biggest source of systematics, but also the solar axion flux uncertainties and the background systematic of the NuSTAR detector. We obtain that the combined effect of these systematics can either improve our limit on $g_{a\gamma}$ by 20.4% or worsen it by 27.3%. We, therefore, consider our approach appropriate and conservative.

Results and Discussion

With the statistical analysis described above, the solar axion observation data of NuSTAR provides a constraint of $6.9 \times 10^{-12} \text{ GeV}^{-1}$ at the 95% CL on the axion–photon coupling strength $g_{a\gamma}$ for axion masses $m_a \lesssim 2 \times 10^{-7} \text{ eV}$. The limit is shown in blue in the wider $m_a - g_{a\gamma}$ landscape of Fig. 6. While NuSTAR’s limits are nearly independent of the axion mass for $m_a \lesssim 2 \times 10^{-7} \text{ eV}$, they weaken for larger masses due to the loss of coherence in the conversion probability described in Eq. (2), i.e., when the axion mass exceeds the plasma frequency at relatively low solar atmosphere heights.

In Fig. 6, the NuSTAR limits are compared to past and future ground-based axion helioscopes (horizontal lines). These experiments look for a signature similar to the one discussed in this work but make use of strong laboratory magnets for axion-photon conversion. Their advantage is clearly the possibility of controlling the magnetic field

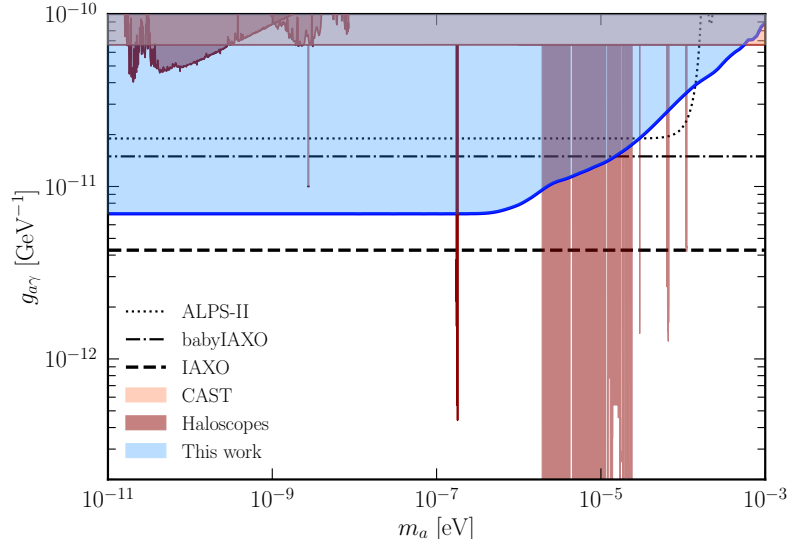


Fig. 6: NuSTAR’s 95% CL exclusion on the $g_{a\gamma}$ coupling strength (blue line). Regions excluded by this work are shown in shaded blue. We show existing bounds from haloscopes [28, 73–100] (in dark red) and the CAST helioscope [21–26] (in light red). We additionally show sensitivity forecasts for the light-shining-through-walls experiment ALPS-II [101] and future helioscopes BabyIAXO and IAXO [29, 102, 103].

and plasma frequency in the laboratory, whilst, in the case of the Sun, these are given. On the other hand, the Sun is an extremely well-studied target, and, contrary to many other celestial objects, this allows us to narrow down the systematic uncertainty associated with the magnetic field model at a level that it does not represent a major issue for the axion bounds (see also Supplemental). At low axion masses, the NuSTAR limit provides a dramatic improvement over the CAST constraint [26] (light red), and it is in between the future babyIAXO [102] (dashed-dotted, data-taking scheduled to start in 2028) and IAXO [29] (dashed, expected in the 2030’s) experiments. Still, terrestrial helioscopes can cover the relevant range of meV axion masses, which, due to the properties of the solar plasma and magnetic field, is difficult to constrain with observations from X-ray satellites.

Contrary to haloscope experiments [28, 73–100], helioscopes, and thus our work, do not assume axions to be dark matter, since the axion flux is inevitably produced by the Sun. For consistency, the luminosity associated with the axion flux has to be only a small fraction of the total solar luminosity in order to avoid large energy losses due to axion escape [104]. The measured solar neutrino flux and helioseismology require $g_{10} \lesssim 4.1$ [105]. The bounds reported here are well below this limit. In this regime, the precision in the theoretical computation of the axion flux is at the few percent level [106], as discussed above and in the Supplemental. Therefore, it does not represent a major systematic issue. This is important when limits are compared to experiments such as light-shining-through-walls, where the initial photon flux is

instead produced in the laboratory. In Fig. 6, we report the projected sensitivity of ALPS-II laser propagation experiment at DESY [101] (dotted line), for comparison.

We note that there is a wide range of masses where the NuSTAR analysis presented here explores the $m_a - g_{a\gamma}$ parameter space with unprecedented sensitivity, beyond the reach of any near future helioscopes, haloscopes, or light-shining-through-walls experiment, setting the limit at $g_{10} \lesssim 0.07$.

There are other astrophysical probes with sensitivity at the level of the NuSTAR limit. On the other hand, as discussed in the Supplemental Material, those bounds on axions can be derived only with a higher level of systematic uncertainty associated with the modeling of the expected signal.

Further observations with NuSTAR might help to tighten the bound. Simple additional observing time is not expected to play a major role since the bound on $g_{a\gamma}$ scales with $t^{-1/8}$.

Then, and probably most importantly, X-ray observations near a solar eclipse can allow us to include a more accurate Sun’s magnetic field model, possibly leading to higher expected X-ray flux. In this work, we have been conservative about the magnetic field strength, disregarding, e.g., small-scale features that can be mapped with higher precision if the X-ray observations are performed simultaneously with white light corona and photospheric magnetic field observations.

The reported NuSTAR bound and, more generally, the technique of using an X-ray satellite as an axion haloscope are likely to become a standard in the axion quest.

The data supporting the plots in this paper and other findings of this study are available from the corresponding authors upon request.

Acknowledgements

We thank the NuSTAR operations, software, and calibration teams for their support with the execution and analysis of these observations. We would also like to thank Georg G. Raffelt for useful discussions and Jiří Štěpan for his advice about solar magnetic field modeling. ET, MR, and MT acknowledge support from the project “Theoretical Astroparticle Physics (TAsP)” funded by the INFN and from the “Grant for Internationalization” of the University of Torino. MT acknowledges the research grant “Addressing systematic uncertainties in searches for dark matter No. 2022F2843L” funded by MIUR. ET thanks the University of Zaragoza for its hospitality during the initial phases of this work. Part of this work was performed under the auspices of the US Department of Energy by Lawrence Livermore National Laboratory under Contract No. DE-AC52-07NA27344. This article/publication is based upon work from COST Action COSMIC WISPerS CA21106.

Supplementary Information

This Supplementary Information file contains data and additional methods in support of the paper.

A Conversion probability

To determine the axion-photon conversion probability, we use the ingredients described in the previous Sections, and we numerically integrate Eq. (2) up to an altitude $h = 29R_\odot$, which is the upper boundary of our model. In order to illustrate the contribution of different layers of the solar atmosphere, in Fig. 7, we show the conversion probability as a function of the altitude above the photosphere, as if the conversion would stop at h and the photons were then detected by NuSTAR. We show this quantity for several axion masses at an energy of $E = 4$ keV and for a coupling $g_{a\gamma} = 10^{-10}$ GeV $^{-1}$.

At altitudes $h < 10^{-4}R_\odot$, the conversion probability does not grow because of a lack of coherence ($qh \gg 1$), and the X-ray emission is suppressed. The conversion probability starts to grow in correspondence with the plasma density dropping. In fact, when this happens, and as long as the axion mass is negligible compared to the plasma frequency, the phase $\varphi = \int dh q$ becomes approximately constant and factors out in Eq. (2). At the same time, absorption is reduced, and the conversion becomes effective.

When the plasma frequency crosses the axion mass, i.e., the resonance condition, $q = (\omega_p^2 - m_a^2)/2E$ changes sign and is dominated by the axion mass contribution. After this point, the complex oscillation of the phase φ becomes relevant again in Eq. (2), especially for larger axion masses, which lead to smaller oscillation wavelengths. This effect and the decrease of the magnetic field lead to a flattening of the growth of the conversion probability. Since the plasma frequency is never smaller than 10^{-9} eV, see Fig. 3, in the range of altitudes explored by our model, for $m_a \lesssim 10^{-9}$ eV, the resonance condition is not fulfilled. For such masses, the conversion probability flattens in correspondence with the drop of the magnetic field in the corona. Note that for low axion masses, the contribution function for photon production, dP/dh , actually peaks in the middle and upper corona. We conservatively ignore the photon production at still greater heights, ranging up to 1 AU.

Fig. 4 shows the expected photon flux from our signal region $R < 0.1R_\odot$. To better visualize the flux for $m_a > 10^{-5}$ eV, Fig. 8 displays the X-ray spectra for several axion masses. For the largest axion mass shown, $m_a = 4 \times 10^{-3}$ eV, the effect of photoelectric absorption is clearly visible. In particular, we see an increased absorption for X-ray photons with energy larger than the K-edge energy of iron at 7.112 keV. For the axion masses for which our results surpass those of CAST, the presence of K-edges is, however, irrelevant.

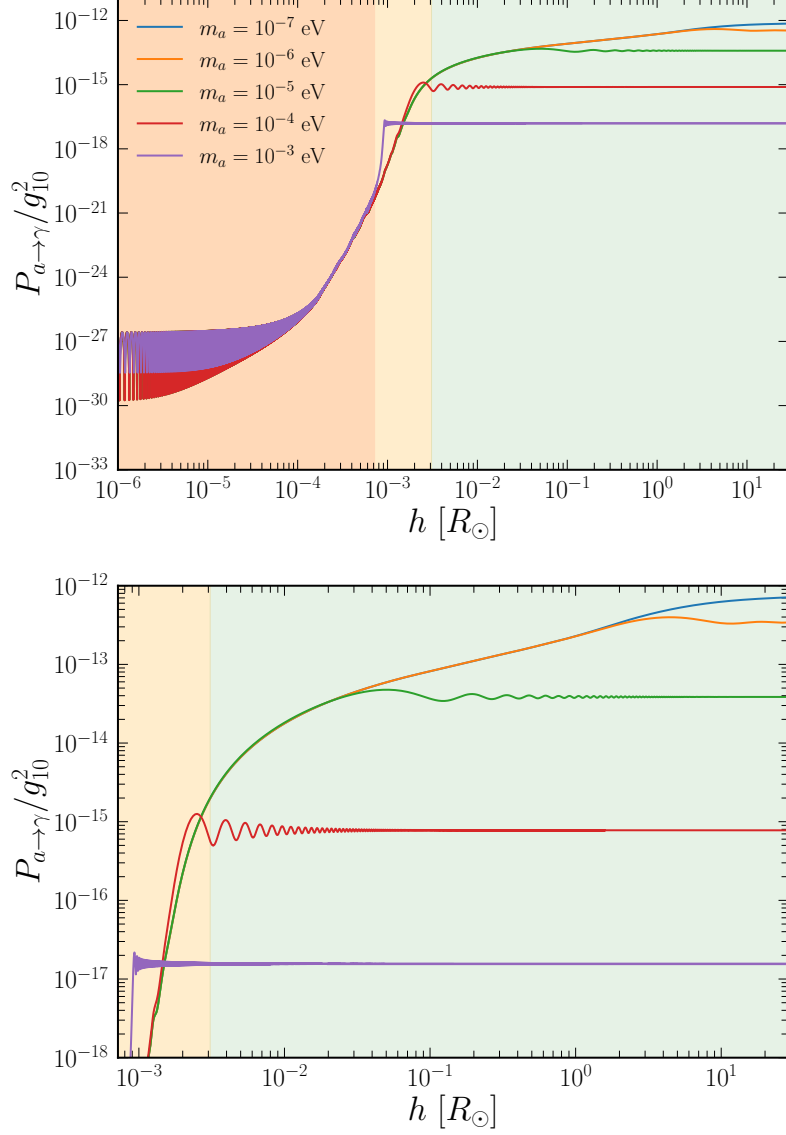


Fig. 7: Top: Overview of the conversion altitude for different axion masses ranging from 10^{-7} to 10^{-3} eV. Curves for lower axion masses are not shown because they would be superimposed to the curve for $m_a = 10^{-7}$ eV. This saturation is reflected in our X-ray spectrum (see Fig. 4) and bound becoming independent of the axion mass from $m_a \lesssim 10^{-7}$ eV. The photosphere, chromosphere, and corona regions of our Sun’s atmosphere are shown in orange, yellow, and green, respectively. **Bottom:** Closeup of the chromosphere and corona, where the probability of conversion is maximized.

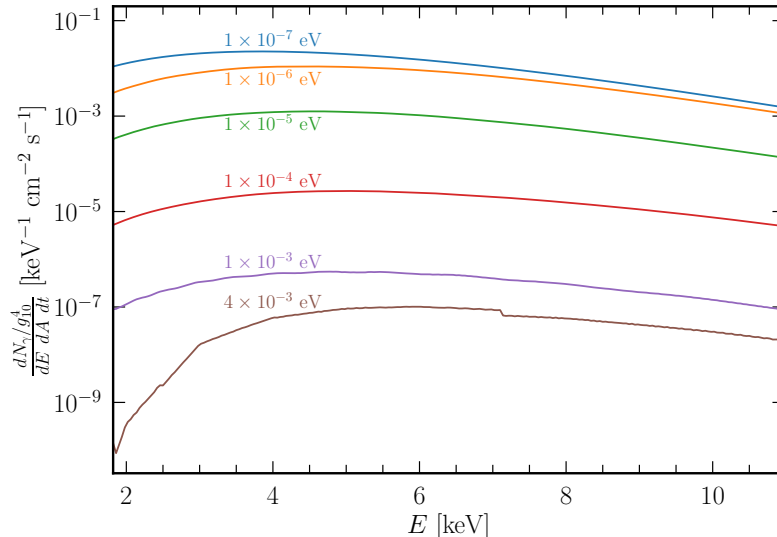


Fig. 8: X-ray spectra reaching NuSTAR satellite depending on axion mass. Notice how the K-shell absorption due to iron presence in our Sun happens for considerably large axion masses $m_a \gtrsim 10^{-3}$ eV. These axions fulfill coherence of conversion in deeper layers than the chromosphere, and their overall flux contribution is considerably smaller (4 orders of magnitude less) than in the case of $m_a \sim 10^{-7}$ eV.

B Experiment and Data Acquisition

B.1 NuSTAR’s Solar Observation Campaigns

NuSTAR has observed the Sun several times since 2014, and an overview of these with quick-look plots is available at [107]. These have predominantly targeted weakly flaring active regions, often not at disk center [69, 108], and so have not been optimal for axion searches. Even when NuSTAR points at quieter regions of the solar disk, stray X-rays that experience only one reflection in the two-stage optics, called “ghost rays,” can still be detected from active regions outside the $12' \times 12'$ field of view [69]. Thus, the whole solar disk needs to be quiet for optimal axion searches. The minimum in the 11-year solar activity cycle hence provides a unique opportunity to study the quiet Sun emission, and NuSTAR had several campaigns targeting it through 2018–2020. Of these, the 21-Feb-2020 campaign is the best for axion work as it is a long dwell at the disk center, during a period of very low solar activity, 9 orbits of observations producing about 23.3 ks of data in each of the two NuSTAR telescope modules. Even during this time, there are faint X-ray features in the solar atmosphere, X-ray bright points, detailed analysis of which are presented in [108]. These features have spectra consistent with optically-thin thermal emission sources. In the majority, the effective temperature of this emission is ≤ 3 MK (with occasional short-lived brightening closer to 4MK). Such sources produce X-ray spectra very sharply decreasing with photon energy, and essentially undetectable above other background sources above 4–5 keV.

There are other NuSTAR solar disk center observations from the time during this solar minimum, but these were taken as part of mosaics of the whole solar disk, such that they only constitute about 100s (0.1 ks) of data. The next solar minimum is not until ~ 2030 , therefore the 2020 NuSTAR observations are the best available X-ray satellite data for axion analysis.

B.2 Processing NuSTAR data for solar observations

NuSTAR collected quiet Sun data over nine spacecraft orbits from 04:51 GMT to 22:41 GMT on February 21, each orbit yielding observations of less than one hour each. Its 12' square field of view (FOV) captured 18% of the solar disk. Although the satellite orbit was chosen to minimize the effects of passage through the South Atlantic Anomaly (SAA) [17], most observations contained observational gaps or dead times due to such passages. The SAA is a geomagnetic anomaly where a weakened magnetic field in the southern area of the Atlantic Ocean exposes spacecraft like NuSTAR in low-Earth orbit to Earth's inner radiation belt at altitudes all the way down to the upper reaches of the atmosphere [109].

Because the Sun drifted slowly across the FOV during data collection, we adjusted the coordinates of the solar center data collection region in 10 to 15-minute intervals to minimize the effects of this drift. Separate data files were extracted for each interval of each orbit. Information about each orbit can be found in Table 1.

Observation No.	ID	On-Target (GMT)	Time (min)	Correction
1	80512218001	05:16:13 - 06:15:48	59.6	0.934
2	80512220001	08:38:10 - 09:29:06	50.9	0.962
3	80512221001	10:06:09 - 10:09:56	47.2	0.965
		10:22:18 - 11:05:44		
4	80512222001	11:42:48 - 11:51:42	45.3	0.981
		12:06:02 - 12:42:23		
5	80512223001	13:19:26 - 13:33:56	44.2	0.974
		13:49:18 - 14:19:02		
6	80512224001	14:56:05 - 15:16:44	43.9	0.960
		15:32:30 - 15:55:40		
7	80512225001	16:32:44 - 17:00:28	44.6	0.981
		17:15:26 - 17:32:19		
8	80512226001	18:09:22 - 18:46:09	47.8	0.999
		18:57:58 - 19:08:58		
9	80512228001	21:22:39 - 22:22:15	59.6	0.945

Table 1: Basic information for each orbit of solar data collected on February 21, 2020, with NuSTAR. Orbits with two time intervals were interrupted by a period of passage through the SAA. The last column shows the scaling factor by which the background collected in the outer annulus region was multiplied to account for the known gradient of stray light background across the chip.

The data were processed using the NuSTAR Data Analysis Software (NuSTAR-DAS) version 2.0.0 to produce scientific products. NuSTARDAS is integrated into the NASA-HEASARC HEASoft software frame (version 6.28), which we downloaded along with the CALDB calibration database (version 20209012) [110]. There were three major data processing steps: data calibration, data screening, and product extraction.

All 32 NuSTAR grades of data were collected without filtering, where each grade represents a unique pattern of energy deposition across the pixels [110]. This produced level 0 data, raw telemetry packets which were then formatted to Level 1 FITS files prior to the calibration step. We processed Level 1 data through the software module *nupipeline* to produce Level 1a calibrated files and Level 2 calibrated and cleaned files. Calibration involves processes including, but not limited to, *nuhotpix*, (searching for hot pixels), *nucalcpa* (assigning each event an energy and grade), and *nucoord* (conversion of raw coordinates to detector and sky coordinates). Screening (also referred to as cleaning) involves processes such as *nucalcsaa* (calculation of SAA passages), *nulivetime* (correction of event file dead times), and *nusplitsc* (splitting of cleaned event files into separate files for each time the spacecraft switched which cameras were used for attitude determination).

The initial processing was followed by selection of the source and background regions. The source region is a circle centered at the solar disk center with radius $0.1R_{\odot}$ (1.6'), and the background region is an annulus from 0.15 to 0.30 solar radii. Wedges were occasionally excluded from the background annulus where examination of the energy range from 3.5-4.0 keV showed an X-ray bright point. Generally, no obvious excess was visible above 4.0 keV, but we removed these regions in case their aggregate contained a slight excess not clearly visible in any one image. This method avoids bias by not using the data that actually contribute to the analysis (>4.0 keV) to decide what areas to excise. The editing of the annulus region was done separately for each 10–15 min sub-interval of each orbit. Figure 9 shows the signal and background regions superimposed on data for all the intervals of one orbit.

The first part of the entire *nuproducts* product extraction sequence includes the following functions: *nuproducts* extracting refined PHA files and light curves by slicing out our chosen time intervals and the shapes of our supplied region files; 'numkarf', creating ancillary response files (ARFs) which detail the telescope modules' responses as a function of position on the detectors and energy; and 'numkrmf', creating redistribution matrix files (RMFs) which detail the detectors' response as a function of photon energy. We executed *nuproducts* for each source and background region by supplying directories, IDs, event files, region files, time interval files, and setting automatic background scaling and extraction to 'no'.

The second part of the *nuproducts* sequence is called 'nubackscale', where we extracted our own background scaling variables separately. These variables define what proportion our source and background regions are of the entire FOV without hot/bad pixels and detector gaps. We executed 'nubackscale' by supplying the PHA files of both the source and background from the previous step as well as other reference files pertaining to the observation ID. This added a BACKSCAL keyword to new PHA files, which we used in follow-on steps.

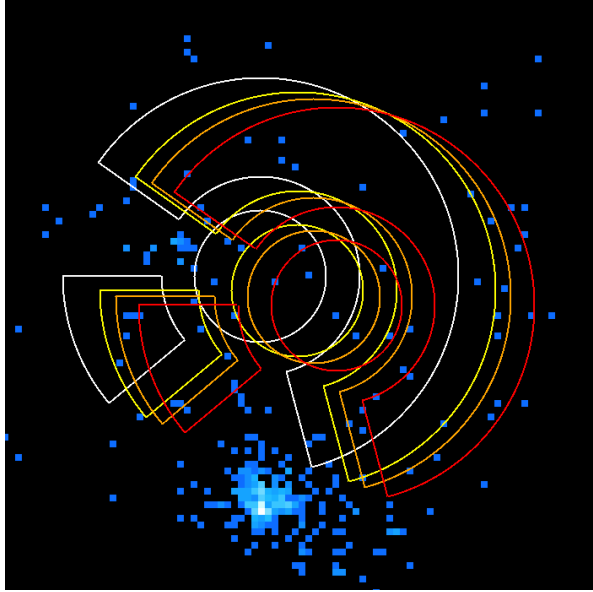


Fig. 9: Data extraction regions for orbit 80512226001, telescope module A. Colour scale: counts from 3.5-4.0 keV, binned to 4x4 detector pixels; darkest blue = 1 count, white = 53 counts. The inner circles are the extraction regions for the disk center source (1.6' radius), and the outer annulus segments are the background extraction region, avoiding the solar X-ray bright point at the bottom of the image and the faint one at the upper left. The contours running from red to white were used sequentially during this orbit to track the motion of the Sun on the sky.

“Stray light” (cosmic diffuse X-rays that enter the detector without encountering the optics) is our dominant source of background and has a distinctive gradient pattern across the detector plane, based on variable shadowing by the spacecraft structure and optics [111]. Using the *nuskybgd* package, we determined the effect of this pattern on each of our source and background annulus regions. On average, the stray light background per detector pixel should have been 0.965 times as high in the source (signal) region than in the background annuli; thus, we scaled down the background calculated in Equation 8 by this factor.

C Sensitivity of the results to model uncertainties

C.1 Coronal modeling for NuSTAR axions

To model the axion conversion in the solar atmosphere, we need estimates of the full magnetic structure of the corona. This can be done with an MHD model based upon the photospheric magnetic observations, and we are lucky to have access to the Predictive Sciences model for the 2-July-2019 total eclipse epoch, as described in [56].

Note that this model describes an epoch a few months before the NuSTAR observations on 21-Feb-2020, and there has been some evolution. One can see a reduction in solar activity from the two *Hinode* X-Ray Telescope snapshots in Fig. 10. This isolated active region was facing Earth at the time of the eclipse and is the only activity present in the three-dimensional PSI model we are considering.

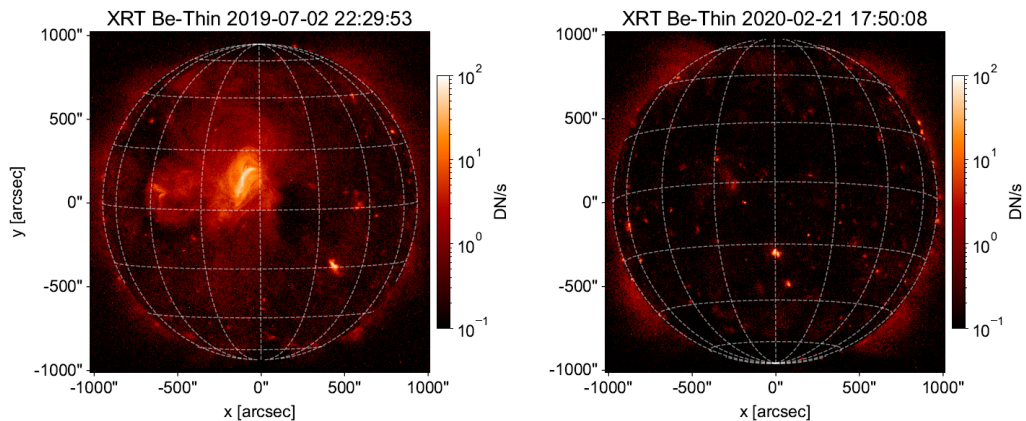


Fig. 10: Soft X-ray images of the full solar disk from the *Hinode* X-Ray Telescope [112, 113]. The 2019 image (left) shows an active region near the disk center. The image at the right, during the NuSTAR observations, shows only a few X-ray bright points, the brightest of which is the one that also appears near the bottom of Figure 9.

Based on SDO’s Helioseismic and Magnetic Imager (SDO/HMI) magnetograms from these two times, the standard Potential-Field Source-Surface (PFSS) magnetic extrapolation can show us what the “magnetic skeleton” of the solar corona looks like. The PFSS model mathematically constructs a global magnetic model by assuming a potential field – this allows no currents to thread the corona as must physically happen, but it captures their presence by an ingenious ad hoc requirement that the field becomes radial at $2.5 R_{\odot}$. The artificial surface currents at this “source surface” simultaneously modify the interior field in a reasonable imitation of the photospheric sources (magnetic active regions, often with sunspots) and also allow for a solar wind (the radial field). Note that the field in the vicinity of the source surface will be greatly distorted.

These models are available online and can help us visualize the evolution of the corona between the PSI model date and that of the NuSTAR data. To check the soundness of the magnetic field model we use in our fiducial analysis (see Figure 3, we compute $|B_{\perp}|$ within the disk of radius $0.1 R_{\odot}$ facing Earth at the time of observation in the PFSS model. We can see from Figure 11 that the two models are in agreement, increasing our confidence in our result.

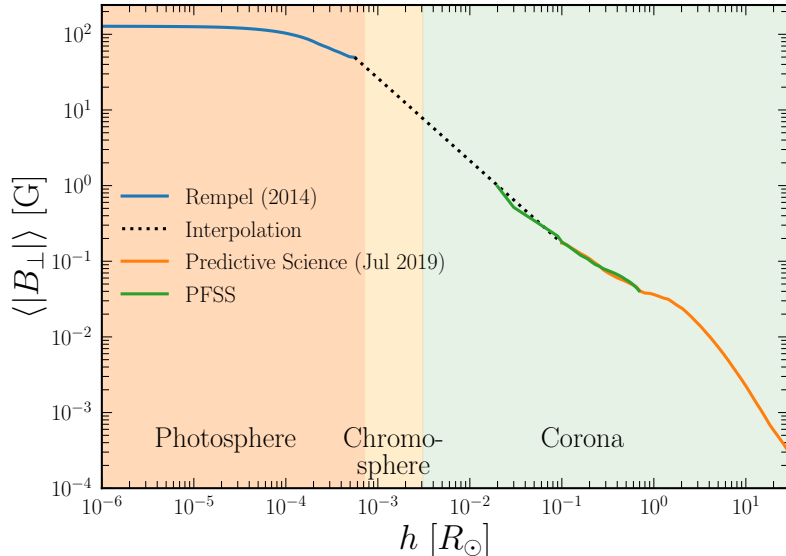


Fig. 11: Our fiducial magnetic field model (blue, dashed black, and orange) derived from the PSI simulation for the 2019 eclipse in comparison to the PFSS model for the day of NuSTAR observations (green). The two models are in excellent agreement in the range of altitudes where the PFSS result is reliable.

C.2 Systematic uncertainties

Sources of systematic uncertainty on our bounds are the solar magnetic field, the solar axion flux, and the NuSTAR background. We first study how our bounds change as we vary the profile shape and the normalization of the coronal magnetic field model. Our photospheric model is already a conservative estimate given that it is representative of the inter-network regions of the quiet Sun, without contributions from network and active regions.

To estimate the uncertainty coming from the profile shape of the coronal magnetic field, we recompute our bound in the limit of vanishing axion mass for 120 profiles obtained by successively rotating the model by 3° angle, as described in the main text. The bounds for larger axion masses will be affected to a lesser extent by changes in the coronal magnetic field, as can be seen from Fig. 7. For each orientation, we average over a perpendicular disk of radius $0.1R_{\odot}$. To isolate the dependence on the shape, we rescale each profile such that $\langle |B_{\perp}| \rangle$ at an altitude $h = 0.1R_{\odot}$ matches that of our fiducial model. Notice that this also agrees with the PFSS model for the day of observation. We re-calculate the bound for each of the 120 profiles and report the systematic error in Table 2 as the percent variation of the bound that corresponds to the 16% and 84% percentiles.

The uncertainty due to the coronal magnetic field’s normalization is estimated from the PFSS model’s variance over the perpendicular disk of radius $0.1R_{\odot}$ at an altitude $h = 0.1R_{\odot}$. The value of $\langle |B_{\perp}| \rangle$ at this altitude is 0.174 G in our reference

Quantity	Systematic effect on $g_{a\gamma}$	
Coronal $\langle B_{\perp} \rangle$ shape	-18%	+26%
Coronal $\langle B_{\perp} \rangle$ normalization	-9.3%	+7.9%
Solar axion flux	-1.5%	+1.5%
NuSTAR background	-1.5%	+1.6%

Table 2: Sources of systematic uncertainty and their effect on our bound for vanishing axion mass.

model. From the PFSS we estimate the 1σ interval $0.141 \text{ G} < |B_{\perp}| < 0.210 \text{ G}$. The variance estimated for this altitude is larger than the variance for $h > 0.1R_{\odot}$ and $h = 0.1R_{\odot}$ is the lowest altitude for which we use the coronal model from PSI. For our error estimate, we rescaled our fiducial magnetic field by an overall factor, such that its value at $h = 0.1R_{\odot}$ is either 0.141 or 0.210 G. Changing the magnetic field in this range yields the percent change in the bound reported in Table 2.

Another source of uncertainty is the solar axion flux. Ref. [106] quotes a systematic uncertainty of 6% due to the solar model. Such an overall rescaling impacts our bounds in a minor way, as shown in Table 2. Additionally, we have considered a potential background dependency due to the Cosmic X-ray Background. However, no such effect was detected within the statistical limits of the NuSTAR data utilized. Nevertheless, based on previous systematic studies of the NuSTAR apparatus [114], we account for the possibility that the background may have been misestimated by a factor of $\pm 1.5\%$. The last line of Table 2 shows how our bound for $m_a \rightarrow 0$ is affected if the photon counts in the annulus are increased or decreased by that quantity.

D Comparison to astrophysical bounds

In addition to the limits presented in Fig. 6, other competitive, but also more model-dependent, astrophysical bounds on the axion-to-photon coupling $g_{a\gamma}$ have been reported in the literature. We show them in Fig. 12. The limits presented in light green arise from a variety of observations. More in detail, Refs. [30–37] searched for the imprint of the axion-photon mixing in the measured energy spectra of extra-galactic gamma-ray and X-ray sources. They require some assumptions concerning the regular and turbulent components of the magnetic field where the conversion occurs. Other interesting targets exploited to constrain the axion-photon conversion are super-giant stars [38], stars in external galaxies [39], magnetic white dwarfs [40, 41], pulsars [42], super star clusters [43] and the supernova SN1987A [44, 45]. While being excellent targets for axion searches, these systems have uncertainties on the magnetic field and plasma density that can be significant, impacting the associated bounds.

The astrophysical bounds shown in purple in Fig. 12 from neutron stars [46, 47] or from the explosion of hypothetical axion stars [48], assume that all the dark matter is in the form of axions. On the contrary, the limits derived in this paper, as well as the previously discussed bounds, do not rely on this assumption. Finally, the dark green area in Fig. 12 corresponds to the limits from globular clusters derived from the R

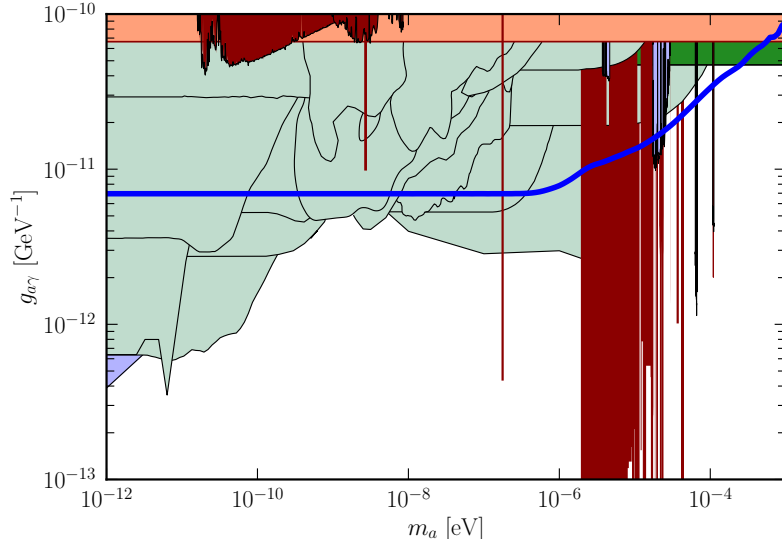


Fig. 12: NuSTAR’s 95% CL upper limit on the axion–photon coupling strength $g_{a\gamma}$ from our work (blue line). Bounds from haloscopes [28, 73–100] are shown in dark red while the CAST helioscope constraint [21–26] is in light red. The dark green area corresponds to the limits from globular clusters derived from the R parameter [115], while the light green regions are the astrophysical bounds derived in [30–45]. The astrophysical bounds in purple from [46–48] rely on the assumption that all the dark matter is in the form of axions. The code to generate this plot was adapted from <https://github.com/cajohare/AxionLimit>.

parameter [115], which measures the number ratio of horizontal branch over red giant stars in globular clusters. The level of this bound is similar to the one obtained from the R_2 parameter [116], the ratio of stellar populations on the asymptotic giant branch to the horizontal branch.

As shown in Fig. 12, several of the methods discussed in this Section appear quite promising in the search for axions. On the other hand, the associated limits entail quite larger levels of uncertainty when compared to the constraints derived in this work and those shown in Fig. 6. As mentioned above, this is mainly related to the modeling of the axion production and conversion in the above astrophysical targets, a task that is often quite complex and relies on parameters that might not be precisely known.

In this respect, the search conducted in this paper presents an advantage because the Sun provides an environment where model uncertainties can be conservatively estimated, enabling the extraction of reliable and tight bounds on axions.

References

- [1] Peccei, R. D. & Quinn, H. R. CP conservation in the presence of pseudoparticles. *Physical Review Letters* **38**, 1440–1443 (1977). URL <https://doi.org/10.1103/PhysRevLett.38.1440>.
- [2] Weinberg, S. A new light boson? *Phys. Rev. Lett.* **40**, 223–226 (1978). URL <https://link.aps.org/doi/10.1103/PhysRevLett.40.223>.
- [3] Wilczek, F. Problem of strong p and t invariance in the presence of instantons. *Phys. Rev. Lett.* **40**, 279–282 (1978). URL <https://link.aps.org/doi/10.1103/PhysRevLett.40.279>.
- [4] Abbott, L. & Sikivie, P. A cosmological bound on the invisible axion. *Physics Letters B* **120**, 133–136 (1983). URL <https://www.sciencedirect.com/science/article/pii/037026938390638X>.
- [5] Preskill, J., Wise, M. B. & Wilczek, F. Cosmology of the Invisible Axion. *Phys. Lett.* **B120**, 127–132 (1983). URL [https://doi.org/10.1016/0370-2693\(83\)90637-8](https://doi.org/10.1016/0370-2693(83)90637-8).
- [6] Dine, M., Fischler, W. & Srednicki, M. A Simple Solution to the Strong CP Problem with a Harmless Axion. *Phys. Lett.* **104B**, 199–202 (1981). URL [https://doi.org/10.1016/0370-2693\(81\)90590-6](https://doi.org/10.1016/0370-2693(81)90590-6).
- [7] Dine, M. & Fischler, W. The Not So Harmless Axion. *Phys. Lett.* **B120**, 137–141 (1983). URL [https://doi.org/10.1016/0370-2693\(83\)90639-1](https://doi.org/10.1016/0370-2693(83)90639-1).
- [8] Chou, A. S. *et al.* Snowmass Cosmic Frontier Report (2022). [2211.09978](https://arxiv.org/abs/2211.09978).
- [9] Adams, C. B. *et al.* Axion Dark Matter (2022). [2203.14923](https://arxiv.org/abs/2203.14923).
- [10] Antel, C. *et al.* Feebly-interacting particles: FIPs 2022 Workshop Report (2023). [2305.01715](https://arxiv.org/abs/2305.01715).
- [11] Sikivie, P. Experimental Tests of the Invisible Axion. *Phys. Rev. Lett.* **51**, 1415–1417 (1983). URL <https://doi.org/10.1103/PhysRevLett.51.1415>.
- [12] Carlson, E. D. & Tseng, L.-S. Pseudoscalar conversion and x-rays from the sun. *Phys. Lett. B* **365**, 193–201 (1996). URL [https://doi.org/10.1016/0370-2693\(95\)01250-8](https://doi.org/10.1016/0370-2693(95)01250-8).
- [13] Tsuneta, S. *et al.* The soft X-ray telescope for the SOLAR-A mission. *Solar Physics* **136**, 37–67 (1991). URL <https://doi.org/10.1007/BF00151694>.
- [14] Hannah, I. G., Hurford, G. J., Hudson, H. S., Lin, R. P. & van Bibber, K. First Limits on the 3-200 keV X-Ray Spectrum of the Quiet Sun Using RHESSI. *ApJL* **659**, L77–L80 (2007). URL <https://doi.org/10.1086/516750>.

- [15] Hannah, I. G., Hudson, H. S., Hurford, G. J. & Lin, R. P. Constraining the hard X-ray properties of the quiet Sun with new RHESSI observations. *ApJ* **724**, 487–492 (2010). URL <https://doi.org/10.1088/0004-637X/724/1/487>.
- [16] Hudson, H. S., Acton, L. W., DeLuca, E. E. & *al.* Bellot Rubio, L., Reale, F. & Carlsson, M. (eds) *X-Ray Searches for Solar Axions*. (eds Bellot Rubio, L., Reale, F. & Carlsson, M.) *4th Hinode Science Meeting: Unsolved Problems and Recent Insights*, Vol. 455 of *Astronomical Society of the Pacific Conference Series*, 25 (2012). URL <https://doi.org/10.48550/arXiv.1201.4607>.
- [17] Harrison, F. A. *et al.* The nuclear spectroscopic telescope array (nustar) high-energy x-ray mission. *The Astrophysical Journal* **770**, 103 (2013). URL <https://dx.doi.org/10.1088/0004-637X/770/2/103>.
- [18] *Nuclear Spectroscopic Telescope Array*. URL <https://science.nasa.gov/mission/nustar>.
- [19] *CESSI repository for Sun magnetic modeclipse 2020*. URL <http://www.cessi.in/solareclipse2020>.
- [20] Moriyama, S. *et al.* Direct search for solar axions by using strong magnetic field and x-ray detectors. *Physics Letters B* **434**, 147–152 (1998). URL <https://www.sciencedirect.com/science/article/pii/S0370269398007667>.
- [21] Zioutas, K. *et al.* First results from the cern axion solar telescope. *Phys. Rev. Lett.* **94**, 121301 (2005). URL <https://link.aps.org/doi/10.1103/PhysRevLett.94.121301>.
- [22] Andriamonje, S. *et al.* An improved limit on the axion–photon coupling from the cast experiment. *Journal of Cosmology and Astroparticle Physics* **2007**, 010–010 (2007). URL <http://dx.doi.org/10.1088/1475-7516/2007/04/010>.
- [23] Arik, E. *et al.* Probing ev-scale axions with cast. *Journal of Cosmology and Astroparticle Physics* **2009**, 008 (2009). URL <https://dx.doi.org/10.1088/1475-7516/2009/02/008>.
- [24] Arik, M. *et al.* Search for solar axions by the cern axion solar telescope with ^3He buffer gas: Closing the hot dark matter gap. *Phys. Rev. Lett.* **112**, 091302 (2014). URL <https://link.aps.org/doi/10.1103/PhysRevLett.112.091302>.
- [25] Arik, M. *et al.* Search for sub-ev mass solar axions by the cern axion solar telescope with ^3He buffer gas. *Phys. Rev. Lett.* **107**, 261302 (2011). URL <https://link.aps.org/doi/10.1103/PhysRevLett.107.261302>.
- [26] Anastassopoulos, V. *et al.* New cast limit on the axion–photon interaction. *Nature Physics* **13**, 584–590 (2017). URL <https://doi.org/10.1038/nphys4109>.

- [27] Physics: Not a wisp of evidence. *Nature* **465**, 271–271 (2010). URL <https://doi.org/10.1038/465271c>.
- [28] Bartram, C. *et al.* Search for Invisible Axion Dark Matter in the 3.3–4.2 μeV Mass Range. *Phys. Rev. Lett.* **127**, 261803 (2021).
- [29] Armengaud, E. *et al.* Physics potential of the international axion observatory (iaxo). *Journal of Cosmology and Astroparticle Physics* **2019**, 047 (2019). URL <https://dx.doi.org/10.1088/1475-7516/2019/06/047>.
- [30] Li, H.-J., Guo, J.-G., Bi, X.-J., Lin, S.-J. & Yin, P.-F. Limits on axionlike particles from mrk 421 with 4.5-year period observations by argo-ybj and fermi-lat. *Physical Review D* **103** (2021). URL <http://dx.doi.org/10.1103/PhysRevD.103.083003>.
- [31] Li, H.-J., Bi, X.-J. & Yin, P.-F. Searching for axion-like particles with the blazar observations of magic and fermi-lat *. *Chinese Physics C* **46**, 085105 (2022). URL <http://dx.doi.org/10.1088/1674-1137/ac6d4f>.
- [32] Reynolds, C. S. *et al.* Astrophysical limits on very light axion-like particles from chandra grating spectroscopy of ngc 1275. *The Astrophysical Journal* **890**, 59 (2020). URL <http://dx.doi.org/10.3847/1538-4357/ab6a0c>.
- [33] Abramowski, A. *et al.* Constraints on axionlike particles with h.e.s.s. from the irregularity of the pks energy spectrum. *Physical Review D* **88** (2013). URL <http://dx.doi.org/10.1103/PhysRevD.88.102003>.
- [34] Ajello, M. *et al.* Search for spectral irregularities due to photon–axionlike-particle oscillations with the fermi large area telescope. *Physical Review Letters* **116** (2016). URL <http://dx.doi.org/10.1103/PhysRevLett.116.161101>.
- [35] Davies, J., Meyer, M. & Cotter, G. Constraints on axionlike particles from a combined analysis of three flaring flat-spectrum radio quasars. *Physical Review D* **107** (2023). URL <http://dx.doi.org/10.1103/PhysRevD.107.083027>.
- [36] Jacobsen, S., Linden, T. & Freese, K. Constraining axion-like particles with HAWC observations of TeV blazars. *JCAP* **10**, 009 (2023).
- [37] Li, H.-J., Chao, W. & Zhou, Y.-F. Upper limit on axion-photon coupling from Markarian 421 (2024). [2406.00387](https://arxiv.org/abs/2406.00387).
- [38] Xiao, M. *et al.* Constraints on Axionlike Particles from a Hard X-Ray Observation of Betelgeuse. *Phys. Rev. Lett.* **126**, 031101 (2021). URL <https://doi.org/10.1103/PhysRevLett.126.031101>.
- [39] Ning, O. & Safdi, B. R. Leading Axion-Photon Sensitivity with NuSTAR Observations of M82 and M87 (2024). [2404.14476](https://arxiv.org/abs/2404.14476).

- [40] Dessert, C., Dunsky, D. & Safdi, B. R. Upper limit on the axion-photon coupling from magnetic white dwarf polarization. *Physical Review D* **105** (2022). URL <http://dx.doi.org/10.1103/PhysRevD.105.103034>.
- [41] Dessert, C., Long, A. J. & Safdi, B. R. No evidence for axions from chandra observation of the magnetic white dwarf re j0317-853. *Physical Review Letters* **128** (2022). URL <http://dx.doi.org/10.1103/PhysRevLett.128.071102>.
- [42] Noordhuis, D. *et al.* Novel Constraints on Axions Produced in Pulsar Polar-Cap Cascades. *Phys. Rev. Lett.* **131**, 111004 (2023).
- [43] Dessert, C., Foster, J. W. & Safdi, B. R. X-ray searches for axions from super star clusters. *Physical Review Letters* **125** (2020). URL <http://dx.doi.org/10.1103/PhysRevLett.125.261102>.
- [44] Hoof, S. & Schulz, L. Updated constraints on axion-like particles from temporal information in supernova sn1987a gamma-ray data. *Journal of Cosmology and Astroparticle Physics* **2023**, 054 (2023). URL <http://dx.doi.org/10.1088/1475-7516/2023/03/054>.
- [45] Manzari, C. A., Park, Y., Safdi, B. R. & Savoray, I. Supernova axions convert to gamma-rays in magnetic fields of progenitor stars (2024). [2405.19393](https://arxiv.org/abs/2405.19393).
- [46] Foster, J. W. *et al.* Extraterrestrial Axion Search with the Breakthrough Listen Galactic Center Survey. *Phys. Rev. Lett.* **129**, 251102 (2022). URL <https://doi.org/10.1103/PhysRevLett.129.251102>.
- [47] Battye, R. A. *et al.* Searching for time-dependent axion dark matter signals in pulsars. *Phys. Rev. D* **108**, 063001 (2023). URL <https://doi.org/10.1103/PhysRevD.108.063001>.
- [48] Escudero, M. *et al.* Axion star explosions: A new source for axion indirect detection. *Phys. Rev. D* **109**, 043018 (2024). URL <https://doi.org/10.1103/PhysRevD.109.043018>.
- [49] Bahcall, J. N., Huebner, W. F., Lubow, S. H., Parker, P. D. & Ulrich, R. K. Standard solar models and the uncertainties in predicted capture rates of solar neutrinos. *Reviews of Modern Physics* **54**, 767 (1982). URL <https://doi.org/10.1103/RevModPhys.54.767>.
- [50] Raffelt, G. G. *Astrophysical Axion Bounds*, 51–71 (Springer Berlin Heidelberg, Berlin, Heidelberg, 2008). URL https://doi.org/10.1007/978-3-540-73518-2_3.
- [51] Raffelt, G. G. *Stars as laboratories for fundamental physics: the astrophysics of neutrinos, axions, and other weakly interacting particles* (Chicago: University of Chicago Press, 1996, 1996).

- [52] Raffelt, G. & Stodolsky, L. Mixing of the Photon with Low Mass Particles. *Phys. Rev. D* **37**, 1237 (1988). URL <https://doi.org/10.1103/PhysRevD.37.1237>.
- [53] van Bibber, K., McIntyre, P. M., Morris, D. E. & Raffelt, G. G. Design for a practical laboratory detector for solar axions. *Phys. Rev. D* **39**, 2089–2099 (1989). URL <https://link.aps.org/doi/10.1103/PhysRevD.39.2089>.
- [54] Vernazza, J. E., Avrett, E. H. & Loeser, R. Structure of the solar chromosphere. III - Models of the EUV brightness components of the quiet-sun. *ApJS* **45**, 635–725 (1981). URL <https://doi.org/10.1086/190731>.
- [55] Rempel, M. Numerical simulations of quiet sun magnetism: On the contribution from a small-scale dynamo. *The Astrophysical Journal* **789**, 132 (2014). URL <http://dx.doi.org/10.1088/0004-637X/789/2/132>.
- [56] Mikić, Z. *et al.* Predicting the corona for the 21 august 2017 total solar eclipse. *Nature Astronomy* **2**, 913–921 (2018). URL <https://doi.org/10.1038/s41550-018-0562-5>.
- [57] Vögler, A. *et al.* Simulations of magneto-convection in the solar photosphere. Equations, methods, and results of the MURaM code. *A&A* **429**, 335–351 (2005). URL <https://doi.org/10.1051/0004-6361:20041507>.
- [58] Rempel, M., Schüssler, M. & Knölker, M. Radiative Magnetohydrodynamic Simulation of Sunspot Structure. *ApJ* **691**, 640–649 (2009). URL <https://doi.org/10.1088/0004-637X/691/1/640>.
- [59] Trujillo Bueno, J., Shchukina, N. & Asensio Ramos, A. A substantial amount of hidden magnetic energy in the quiet Sun. *Nature* **430**, 326–329 (2004).
- [60] del Pino Aleman, T., Bueno, J. T., Stepan, J. & Shchukina, N. A novel investigation of the small-scale magnetic activity of the quiet sun via the hanle effect in the sr i 4607 Å line. *The Astrophysical Journal* **863**, 164 (2018). URL <https://dx.doi.org/10.3847/1538-4357/aaceab>.
- [61] De La Luz, V., Lara, A., Mendoza, E. & Shimojo, M. 3D Simulations of the Quiet Sun Radio Emission at Millimeter and Submillimeter Wavelengths. *Geofisica Internacional* **47**, 197–203 (2008). URL <https://ui.adsabs.harvard.edu/abs/2008GeofI..47..197D>.
- [62] Gabriel, A. H. A Magnetic Model of the Solar Transition Region. *Philosophical Transactions of the Royal Society of London Series A* **281**, 339–352 (1976). URL <https://doi.org/10.1098/rsta.1976.0031>.
- [63] Schmelz, J. T., Reames, D. V., von Steiger, R. & Basu, S. Composition of the Solar Corona, Solar Wind, and Solar Energetic Particles. *ApJ* **755**, 33 (2012). URL <https://doi.org/10.1088/0004-637X/755/1/33>.

- [64] Caffau, E., Ludwig, H. G., Steffen, M., Freytag, B. & Bonifacio, P. Solar Chemical Abundances Determined with a CO5BOLD 3D Model Atmosphere. *Solar Physics* **268**, 255–269 (2011). URL <https://doi.org/10.1007/s11207-010-9541-4>.
- [65] Lodders, K., Palme, H. & Gail, H. P. Abundances of the Elements in the Solar System. *Landolt Börnstein* **4B**, 712 (2009). URL https://doi.org/10.1007/978-3-540-88055-4_34.
- [66] Dere, K. P., Landi, E., Mason, H. E., Monsignori Fossi, B. C. & Young, P. R. CHIANTI - an atomic database for emission lines. *A&AS* **125**, 149–173 (1997). URL <https://doi.org/10.1051/aas:1997368>.
- [67] Del Zanna, G., Dere, K. P., Young, P. R. & Landi, E. CHIANTI—An Atomic Database for Emission Lines. XVI. Version 10, Further Extensions. *ApJ* **909**, 38 (2021). URL <https://doi.org/10.3847/1538-4357/abd8ce>.
- [68] Berger, M. J. and Hubbell, J. H. and Seltzer, S. M. and Chang, J. and Coursey, J. S. and Sukumar, R. and Zucker, D. S and Olsen, K. NIST Standard Reference Database 8 (XGAM) (2010). URL <https://www.nist.gov/pml/xcom-photon-cross-sections-database>.
- [69] Grefenstette, B. W. *et al.* The first focused hard x-ray images of the sun with nustar. *The Astrophysical Journal* **826**, 20 (2016). URL <https://dx.doi.org/10.3847/0004-637X/826/1/20>.
- [70] Paterson, S. *et al.* Time evolution of X-ray bright points observed with NuSTAR. *Monthly Notices of the Royal Astronomical Society* **528**, 6398–6410 (2024). URL <https://doi.org/10.1093/mnras/stae417>.
- [71] Brejnholt, N. F. *et al.* Takahashi, T., Murray, S. S. & den Herder, J.-W. A. (eds) *NuSTAR on-ground calibration: II. Effective area.* (eds Takahashi, T., Murray, S. S. & den Herder, J.-W. A.) *Space Telescopes and Instrumentation 2012: Ultraviolet to Gamma Ray*, Vol. 8443, 84431Y. International Society for Optics and Photonics (SPIE, 2012). URL <https://doi.org/10.1117/12.925631>.
- [72] Westergaard, N. J. *et al.* Takahashi, T., Murray, S. S. & den Herder, J.-W. A. (eds) *NuSTAR on-ground calibration: I. Imaging quality.* (eds Takahashi, T., Murray, S. S. & den Herder, J.-W. A.) *Space Telescopes and Instrumentation 2012: Ultraviolet to Gamma Ray*, Vol. 8443, 84431X. International Society for Optics and Photonics (SPIE, 2012). URL <https://doi.org/10.1117/12.927076>.
- [73] Asztalos, S. J. *et al.* Squid-based microwave cavity search for dark-matter axions. *Physical Review Letters* **104** (2010). URL <http://dx.doi.org/10.1103/PhysRevLett.104.041301>.
- [74] Du, N. *et al.* Search for invisible axion dark matter with the axion dark matter experiment. *Physical Review Letters* **120** (2018). URL <http://dx.doi.org/10.1103/PhysRevLett.120.041301>.

1103/PhysRevLett.120.151301.

- [75] Braine, T. *et al.* Extended search for the invisible axion with the axion dark matter experiment. *Physical Review Letters* **124** (2020). URL <http://dx.doi.org/10.1103/PhysRevLett.124.101303>.
- [76] Boutan, C. *et al.* Piezoelectrically tuned multimode cavity search for axion dark matter. *Physical Review Letters* **121** (2018). URL <http://dx.doi.org/10.1103/PhysRevLett.121.261302>.
- [77] Bartram, C. *et al.* Dark matter axion search using a josephson traveling wave parametric amplifier. *Review of Scientific Instruments* **94** (2023). URL <http://dx.doi.org/10.1063/5.0122907>.
- [78] Hagmann, C., Sikivie, P., Sullivan, N. S. & Tanner, D. B. Results from a search for cosmic axions. *Phys. Rev. D* **42**, 1297–1300 (1990). URL <https://link.aps.org/doi/10.1103/PhysRevD.42.1297>.
- [79] Zhong, L. *et al.* Results from phase 1 of the haystac microwave cavity axion experiment. *Physical Review D* **97** (2018). URL <http://dx.doi.org/10.1103/PhysRevD.97.092001>.
- [80] Backes, K. M. *et al.* A quantum enhanced search for dark matter axions. *Nature* **590**, 238–242 (2021). URL <http://dx.doi.org/10.1038/s41586-021-03226-7>.
- [81] Collaboration, H. *et al.* New results from haystac’s phase ii operation with a squeezed state receiver (2023). [2301.09721](https://arxiv.org/abs/2301.09721).
- [82] Lee, S., Ahn, S., Choi, J., Ko, B. R. & Semertzidis, Y. K. Axion Dark Matter Search around 6.7 μeV . *Phys. Rev. Lett.* **124**, 101802 (2020).
- [83] Jeong, J. *et al.* Search for invisible axion dark matter with a multiple-cell haloscope. *Physical Review Letters* **125** (2020). URL <http://dx.doi.org/10.1103/PhysRevLett.125.221302>.
- [84] Kwon, O. *et al.* First Results from an Axion Haloscope at CAPP around 10.7 μeV . *Phys. Rev. Lett.* **126**, 191802 (2021).
- [85] Lee, Y. *et al.* Searching for invisible axion dark matter with an 18 t magnet haloscope. *Physical Review Letters* **128** (2022). URL <http://dx.doi.org/10.1103/PhysRevLett.128.241805>.
- [86] Kim, J. *et al.* Near-Quantum-Noise Axion Dark Matter Search at CAPP around 9.5 μeV . *Phys. Rev. Lett.* **130**, 091602 (2023).
- [87] Yi, A. K. *et al.* Axion Dark Matter Search around 4.55 μeV with Dine-Fischler-Srednicki-Zhitnitskii Sensitivity. *Phys. Rev. Lett.* **130**, 071002 (2023).

- [88] Yang, B., Yoon, H., Ahn, M., Lee, Y. & Yoo, J. Extended axion dark matter search using the capp18t haloscope. *Physical Review Letters* **131** (2023). URL <http://dx.doi.org/10.1103/PhysRevLett.131.081801>.
- [89] Kim, Y. *et al.* Experimental search for invisible axions as a test of axion cosmology around 22 uev (2023). [2312.11003](https://arxiv.org/abs/2312.11003).
- [90] Ahn, S. *et al.* Extensive search for axion dark matter over 1 ghz with capp's main axion experiment (2024). [2402.12892](https://arxiv.org/abs/2402.12892).
- [91] Quiskamp, A. *et al.* Direct search for dark matter axions excluding alpogenesis in the 63- to 67- μ ev range with the organ experiment. *Science Advances* **8** (2022). URL <http://dx.doi.org/10.1126/sciadv.abq3765>.
- [92] Quiskamp, A. *et al.* Exclusion of alpogenesis dark matter in a mass window above 100 μ ev (2023). [2310.00904](https://arxiv.org/abs/2310.00904).
- [93] McAllister, B. T. *et al.* The organ experiment: An axion haloscope above 15 ghz. *Physics of the Dark Universe* **18**, 67–72 (2017). URL <http://dx.doi.org/10.1016/j.dark.2017.09.010>.
- [94] Alesini, D. *et al.* Galactic axions search with a superconducting resonant cavity. *Physical Review D* **99** (2019). URL <http://dx.doi.org/10.1103/PhysRevD.99.101101>.
- [95] Alesini, D. *et al.* Search for invisible axion dark matter of mass with the quax experiment. *Physical Review D* **103** (2021). URL <http://dx.doi.org/10.1103/PhysRevD.103.102004>.
- [96] Di Vora, R. *et al.* Search for galactic axions with a traveling wave parametric amplifier. *Physical Review D* **108** (2023). URL <http://dx.doi.org/10.1103/PhysRevD.108.062005>.
- [97] Devlin, J. A. *et al.* Constraints on the Coupling between Axionlike Dark Matter and Photons Using an Antiproton Superconducting Tuned Detection Circuit in a Cryogenic Penning Trap. *Phys. Rev. Lett.* **126**, 041301 (2021).
- [98] Ouellet, J. L. *et al.* First results from abracadabra-10 cm: A search for sub-axion dark matter. *Physical Review Letters* **122** (2019). URL <http://dx.doi.org/10.1103/PhysRevLett.122.121802>.
- [99] Salemi, C. P. *et al.* Search for low-mass axion dark matter with abracadabra-10 cm. *Physical Review Letters* **127** (2021). URL <http://dx.doi.org/10.1103/PhysRevLett.127.081801>.
- [100] Crisosto, N. *et al.* ADMX SLIC: Results from a Superconducting LC Circuit Investigating Cold Axions. *Phys. Rev. Lett.* **124**, 241101 (2020).

- [101] Bahre, R. *et al.* Any light particle search ii — technical design report. *Journal of Instrumentation* **8**, T09001 (2013). URL <https://dx.doi.org/10.1088/1748-0221/8/09/T09001>.
- [102] Abeln, A. *et al.* Conceptual design of BabyIAXO, the intermediate stage towards the International Axion Observatory. *J. High Energ. Phys.* **2021**, 137 (2021).
- [103] Armengaud, E. *et al.* Conceptual Design of the International Axion Observatory (IAXO). *JINST* **9**, T05002 (2014).
- [104] Schlattl, H., Weiss, A. & Raffelt, G. Helioseismological constraint on solar axion emission. *Astroparticle Physics* **10**, 353–359 (1999). URL <https://www.sciencedirect.com/science/article/pii/S0927650598000632>.
- [105] Vinyoles, N. *et al.* New axion and hidden photon constraints from a solar data global fit. *Journal of Cosmology and Astroparticle Physics* **2015**, 015 (2015). URL <https://dx.doi.org/10.1088/1475-7516/2015/10/015>.
- [106] Hoof, S., Jaeckel, J. & Thormaehlen, L. J. Quantifying uncertainties in the solar axion flux and their impact on determining axion model parameters. *JCAP* **09**, 006 (2021).
- [107] *NuSTAR quickplots*. URL <http://ianan.github.io/nsovr>.
- [108] Paterson, S. *et al.* Time evolution of X-ray bright points observed with NuSTAR. *Monthly Notices of the Royal Astronomical Society* **528**, 6398–6410 (2024). URL <https://doi.org/10.1093/mnras/stae417>.
- [109] Dessler, A. J. Effect of magnetic anomaly on particle radiation trapped in geomagnetic field. *Journal of Geophysical Research (1896-1977)* **64**, 713–715 (1959). URL <https://agupubs.onlinelibrary.wiley.com/doi/abs/10.1029/JZ064i007p00713>.
- [110] Perri, M. *et al.* The nustar data analysis software guide.version 1.9.7 (2021). URL https://heasarc.gsfc.nasa.gov/docs/nustar/analysis/nustar_swguide.pdf.
- [111] Wik, D. R. *et al.* Nustar observations of the bullet cluster: Constraints on inverse compton emission. *The Astrophysical Journal* **792**, 48 (2014). URL <https://dx.doi.org/10.1088/0004-637X/792/1/48>.
- [112] Lites, B. W. *et al.* The Horizontal Magnetic Flux of the Quiet-Sun Internetwork as Observed with the Hinode Spectro-Polarimeter. *ApJ* **672**, 1237–1253 (2008).
- [113] Kariyappa, R. *et al.* Temperature variability in X-ray bright points observed with Hinode/XRT. *A&A* **526**, A78 (2011).
- [114] Rosslund, S. *et al.* Measuring the cosmic x-ray background in 3–20 keV with stray light from nustar. *The Astronomical Journal* **166**, 20 (2023). URL <https://doi.org/10.1088/1520-9104/166/1/20>.

[//dx.doi.org/10.3847/1538-3881/acd0ae](http://dx.doi.org/10.3847/1538-3881/acd0ae).

- [115] Ayala, A., Domínguez, I., Giannotti, M., Mirizzi, A. & Straniero, O. Revisiting the bound on axion-photon coupling from globular clusters. *Physical Review Letters* **113** (2014). URL <http://dx.doi.org/10.1103/PhysRevLett.113.191302>.
- [116] Dolan, M. J., Hiskens, F. J. & Volkas, R. R. Advancing globular cluster constraints on the axion-photon coupling. *Journal of Cosmology and Astroparticle Physics* **2022**, 096 (2022). URL <http://dx.doi.org/10.1088/1475-7516/2022/10/096>.